ARTICLE

OBC
www.rsc.org/obc

X–N Charge density analysis of the hydrogen bonding motif in 1-(2-hydroxy-5-nitrophenyl)ethanone †

David E. Hibbs,*[a] Jacob Overgaard[a] and Ross O. Piltz[b]

[a] *School of Chemistry, University of Sydney, Sydney, NSW 2006, Australia. E-mail: d.hibbs@chem.usyd.edu.au; Fax: +61 (0) 2 9351 3329; Tel: +61 (0) 2 9036 9122*

[b] *Neutron Scattering Section, Australian Nuclear Science and Technology Organisation, PMB 1, Menai, NSW 2234, Australia. E-mail: rop@ansto.gov.au; Fax: +61(0) 2 9717 3606; Tel: +61 (0) 2 9717 3607*

Received 25th November 2002, Accepted 3rd February 2003
First published as an Advance Article on the web 3rd March 2003

The total experimental charge density in 1-(2-hydroxy-5-nitrophenyl)ethanone (**1**) has been determined using high-resolution X-ray diffraction data in combination with neutron diffraction data measured at 100 K. Multipole refinement was carried out in terms of the rigid pseudoatom model. Multipole refinement converged at $R = 0.026$ for 5415 reflections with $I > 2\sigma(I)$. Topological analysis of the total experimental charge density $\rho(\mathbf{r})$ and its Laplacian, $-\nabla^2\rho(\mathbf{r})$ together with a comparison against high level theoretical gas-phase calculations reveals fine details of intra- and intermolecular bonding features, in particular the extent of the π-delocalisation throughout the molecule.

Introduction

Flavonoids are polyphenolic compounds found extensively in plants. They are widely known as antioxidants[1] but also influence immune function,[2] gene expression,[3] platelet aggregation[4] and enzyme activity.[5] Recently, it has become clear that some flavonoids have effects on the central nervous system.[6] The molecule 1-(2-hydroxy-5-nitrophenyl)ethanone (**1**) (Fig. 1 and 2), is a synthetic precursor to many poly-substituted synthetic flavones. Our interest in the flavone family is twofold, to understand the small differences in the electronic makeup of structurally similar molecules that confer on this series of compounds a wide range of biological activity, and to determine to what extent the presence of strong intra- and intermolecular interactions can influence this activity.

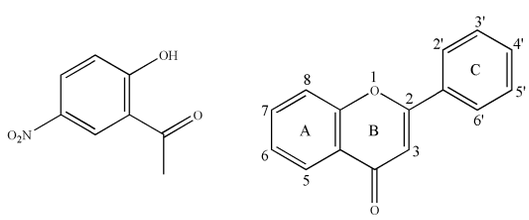

Fig. 1 1-(2-Hydroxy-5-nitrophenyl)ethanone (**1**) (left) and the flavone nucleus (right).

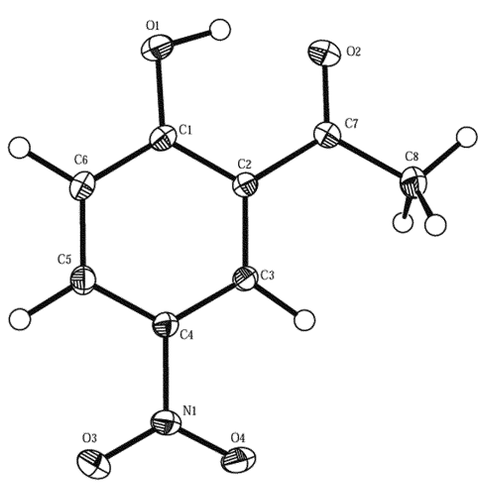

Fig. 2 X-Ray molecular structure of **1**. Ellipsoids are at 90%.

There has been great interest recently in the nature of short hydrogen bonds and their role in biological systems, in particular enzyme catalysis.[7] Very short hydrogen bonds have been suggested to have covalent character based on investigations by a number of experimental techniques,[8,9] but to date there have been surprisingly few experimental charge density studies on such systems.[10] Gilli and co-workers[11] have proposed the resonance assisted hydrogen bonding (RAHB) model to account for very short O–H ··· O and N–H ··· O distances observed in conjugated systems containing hydrogen bonds, and have suggested that this could be related to the π-delocalisation of the O=C–C=C–C–O–H keto–enol group.

It was against this background that we determined the molecular and electronic structure of **1** which has a short intramolecular O–H ··· O hydrogen bond, by a combined X-ray and neutron diffraction study. The neutron diffraction experiment provides the best structural model, and the exact electron distribution was determined using a combined X-ray and neutron (X–N) charge density refinement procedure.

Experimental

Single crystal X-ray data collection ‡

Crystals of **1** were grown from diethyl ether by slow evaporation. Single-crystal, high-resolution, low-temperature data were collected on a Bruker SMART 1000 CCD based diffractometer. Cell constants were obtained from the least squares refinement of 2580 reflections located between 5.36 and 125.16° 2θ. Three reciprocal space data shells were collected, with one shell providing data between 2 and 58° 2θ, a second for data between 42 and 98° 2θ and a third for data between 72 and 128°

† Electronic supplementary information (ESI) available: multipole population coefficients and pseudoatom parameterization. See http://www.rsc.org/suppdata/ob/b2/b211683a/

‡ CCDC reference numbers 199380 and 199381. See http://www.rsc.org/suppdata/ob/b2/b211683a/ for crystallographic data in .cif or other electronic format.

DOI: 10.1039/b211683a

2θ. Data were collected at 100(2) K with ω-scan increments of 0.3°. 40154 reflections were integrated with the program SAINT+ [12] and merged with the program SORTAV.[13] 690 reflections were discarded as gross outliers, and the remaining 39464 reflections were corrected for absorption with an empirical absorption correction [13] and averaged to give 6469 unique reflections with an average redundancy of 6.0. Only 177 reflections below sin $(\theta)/\lambda$ of 1.24 Å^{-1} were missing, and only 230 reflections were measured only once. The internal agreement of the data was 2.0%.

Neutron diffraction data collection and refinement

The single crystal neutron diffraction data was collected on the 2TANA four-circle diffractometer at the HIFAR reactor located at Lucas Heights, Australia.[14] The crystal was approx. 4 × 2.5 × 1.5 mm in dimensions and was mounted by wrapping it in aluminium foil and gluing the foil to an aluminium pin. The crystal was cooled to 100(2) K using the 2TANA helium closed cycle refrigerator. The reflections were collected and processed into integrated intensities using the ANSTO programs DIFF, DIFFPLOT and PEAKPOS. No significant trend was observed in the intensity of the two standard intensities, and so no time dependent correction was applied to the intensity data.

A total of 2916 independent reflections were measured over a 16 day period in seven shells of increasing 2θ up to a maximum of 95 degrees. The wavelength used was 1.235(1) Å.

Averaging equivalent and Friedel reflections gave 671 unique reflections with R(merge) = 5.6%, R(sigma) = 3.8%.

The X-ray structural parameters formed the basis of the starting model and the atomic positions and anisotropic thermal motion was refined for all atoms, including hydrogens.[15] The X–H bond distances were transferred to the multipolar refinements used against the X-ray data. $R1$ = 0.024, $wR2$ = 0.055. Full details of this refinement appear in the accompanying .cif file.

Molecular orbital calculations

All gas phase DFT calculations were performed at both the experimental and the optimised geometry with the GAUSSIAN98 program package [16] at the 6-311++G** level of theory, using the three parameter hybrid exchange functional of Becke in combination with the gradient corrected exchange-correlation potential of Lee, Yang and Parr (B3LYP).[17] The AIMPAC suite of programs was used for the topological analysis of the theoretical wavefunctions.[18] All calculations were performed on a Silicon Graphics ORIGIN2400 computer.[19]

Structural and multipole refinements

The crystal structure of **1** (Fig. 2) was solved from the X-ray data using the direct methods of the program SHELX-S.[20] The hydrogen atoms were fixed at distances corresponding to the X–H bond lengths obtained from the neutron diffraction study (see above section). The atomic positions and thermal displacement parameters obtained from the neutron data refinement were used as an initial structural basis for a high-angle refinement (sin $\theta/\lambda > 0.8$ Å^{-1}). In subsequent refinements of the aspherical electron density the Hansen–Coppens pseudoatom formalism [21] as implemented in the least squares program XDLSM, part of the program package XD,[22] was used. The atomic scattering factors were taken from International Tables of Crystallography,[23] and the radial functions were those of Clementi and Raimondi.[24]

In a crystal the electron density $\rho(\boldsymbol{r})$ can be described by a sum of aspherical pseudoatoms with nuclear positions $\{\boldsymbol{R}_j\}$:

$$\rho(\boldsymbol{r}) = \Sigma_j \rho_j(\boldsymbol{r} - \boldsymbol{R}_j) \quad (1)$$

with the pseudoatomic density form of:

$$\rho_j(\boldsymbol{r}_j) = P_c\rho_c(\boldsymbol{r}_j) + \kappa'^3 P_v\rho_v(\kappa'\boldsymbol{r}_j) + \sum_{l=0}^{l_{max}}\sum_{m=0}^{l} \kappa''^3 P_{lm} R_l(\kappa''\boldsymbol{r}_j) d_{lmp}(\theta_j,\phi_j) \quad (2)$$

thus each pseudoatom is described by three components, core density, spherical valence density, and the deviation of the pseudoatom density from sphericity.

The core and spherical valence density were composed of Hartree–Fock wave functions expanded over Slater type basis functions, with κ' (the expansion–contraction coefficient which modifies the radial distribution) being refined along with the valence population (P_v). The final term describes the deviation of the pseudoatom density from sphericity, and is represented by deformation functions in the form of density-normalised spherical harmonics d_{lmp}.

The Slater type function $Nr^{n_l}\exp(-\kappa''\zeta r)$, forms the radial term (R_l) for the deformation functions, with an additional radial screening parameter (κ'') being refined. The exponents n_l of the Slater function were chosen so that the maximum of the radial function was at the density peak position ($r_{max} = (n_l/\zeta_l)$).

The multipoles were included in a stepwise fashion, first dipoles (l_{max} = 1), then quadrupoles (l_{max} = 2) and finally octupoles (l_{max} = 3) for all non-hydrogen atoms. Hexadecapoles (l_{max} = 4) refined to significant values for N(1) only. Most hydrogen atoms were treated with one monopole and the asphericity was modelled using a single bond directed dipole, with the exception of H(1) which also included a bond directed quadrupole. Before a final refinement of the multipoles was performed, the radial correction of the aspherical functions (κ'') was refined, with this value being kept constant for all values of l. Only significant data ($F > 3\sigma(F)$) were included as observations. As the molecule crystallises in a non-centrosymmetric space group, the refinement of certain parameters can lead to a change in the phases of the structure factors. This can lead to serious discrepancies in the resulting electron density. This was accounted for by applying a number of constraints in the multipole model, firstly the positional parameters were not refined concurrently with the multipoles, secondly the model was subjected to a number of chemical constraints whereby atoms considered 'chemically equivalent' were constrained to have the same multipole populations. The final refinement (on F^2) gave an overall residual of $R_w(F^2)$ = 0.043, and the residual density in the plane of the molecule is shown in Fig. 3. Crystallographic details are listed in Table 1.

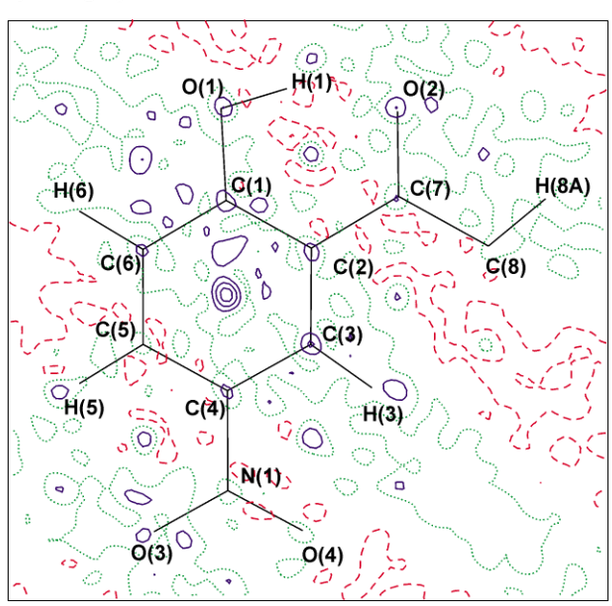

Fig. 3 Residual density map of **1**. Solid blue lines show positive contours, dashed red lines show the negative contours, with the zero contour shown with green dots. Contour levels are 0.1 e Å^{-3} intervals.

Table 1 Final multipole refinement statistics for **1**

Empirical formula	$C_8O_4H_{12}$
Formula weight/g mol^{-1}	181.15
Crystal system	Orthorhombic
Space group	$Pca2_1$
Z	4
Temperature/K	100
a/Å	15.2399(6)
b/Å	7.2338(3)
c/Å	7.277(3)
V/Å^3	802.23(6)
ρ_{calc}/Mg m^{-3}	1.512
$F(000)$	376
μ/mm^{-1}	0.124
Tmax; Tmin	1.000, 0.924
Crystal size/mm	0.30 × 0.25 × 0.25
λ/Å	0.71073
sin $(\theta)/\lambda_{max}$/Å^{-1}	1.24
Limiting indices (h, k, l)	$0 \le 37$; $0 \le 17$; $0 \le 17$
Number of collected reflections	40154
Symmetry independent reflections	6469
Reflections with $I_0 > 2\sigma(I_0)$	5415
Completeness	97%
Redundancy	av. 6.0
R_{int}	0.020
$R(F)$	0.026
$R_w(F^2)$	0.043
S	2.0
Number of variables	188
N_{ref}/N_v	26.3

Table 2 Bond lengths and angles[a] for **1** [Å, °]

C(1)–O(1)	1.342(1)	C(1)–O(1)–H(1)	103.6(1)
C(1)–C(6)	1.407(1)	O(3)–N(1)–O(4)	122.9(1)
C(1)–C(2)	1.423(1)	O(3)–N(1)–C(4)	118.9(1)
C(2)–C(3)	1.403(1)	O(4)–N(1)–C(4)	118.3(1)
C(2)–C(7)	1.478(1)	O(1)–C(1)–C(2)	122.4(1)
C(3)–C(4)	1.389(1)	O(1)–C(1)–C(6)	117.3(1)
C(3)–H(3)	1.095(1)	C(2)–C(1)–C(6)	120.4(1)
C(4)–C(5)	1.403(1)	C(1)–C(2)–C(3)	118.8(1)
C(4)–N(1)	1.456(1)	C(1)–C(2)–C(7)	120.1(1)
C(5)–C(6)	1.384(1)	C(3)–C(2)–C(7)	121.0(1)
C(5)–H(5)	1.089(3)	C(2)–C(3)–C(4)	119.4(1)
C(6)–H(6)	1.081(1)	C(2)–C(3)–H(3)	125.0(2)
C(7)–O(2)	1.241(1)	C(4)–C(3)–H(3)	115.6(2)
C(7)–C(8)	1.501(1)	N(1)–C(4)–C(3)	118.8(1)
C(8)–H(8A)	1.084(3)	N(1)–C(4)–C(5)	119.0(1)
C(8)–H(8B)	1.081(5)	C(3)–C(4)–C(5)	122.2(1)
C(8)–H(8C)	1.085(4)	C(4)–C(5)–C(6)	118.8(1)
N(1)–O(3)	1.233(1)	C(4)–C(5)–H(5)	119.6(2)
N(1)–O(4)	1.235(1)	C(6)–C(5)–H(5)	121.4(1)
O(1)–H(1)	1.000(2)	C(1)–C(6)–C(5)	120.4(1)
		C(1)–C(6)–H(6)	118.5(1)
		C(5)–C(6)–H(6)	121.2(2)
		O(2)–C(7)–C(2)	119.8(1)
		O(2)–C(7)–C(8)	119.9(1)
		C(2)–C(7)–C(8)	120.3(1)
		C(7)–C(8)–H(8A)	111.6(2)
		C(7)–C(8)–H(8B)	106.3(2)
		C(7)–C(8)–H(8C)	114.4(2)
		H(8A)–C(8)–H(8B)	108.6(2)
		H(8A)–C(8)–H(8C)	107.0(5)
		H(8B)–C(8)–H(8C)	108.8(2)

[a] Values taken from the X-ray refinement.

Results and discussion

Details of the molecular geometry from the X-ray refinement are outlined in Table 2. Here the nitro-group has two N–O bonds with identical bond lengths, which indicates complete electronic delocalisation in this part of the molecule. This must be due to very similar chemical environments of the two oxygen atoms, including any hydrogen bonding motifs. However, it appears that O(3) has slightly weaker interactions with its nearest neighbours than O(4). The O(3) ··· H(5) distance is 0.1 Å longer than the O(4) ··· H(3) distance, and the shortest intermolecular hydrogen bond is 2.628(1) Å for O(3) and 2.240(1) Å for O(4) (see hydrogen bonding section). However, the nature of these interactions are so weak that they impose no structural disparity on either N–O bond.

Several methods can be used to examine the interatomic bonding. The traditional method used in charge density studies has been the (static) deformation density method. This technique involves subtracting the superposition of neutral, non-interacting atoms (the Independent Atom Model, IAM) from the observed electron density (or the density described by the multipolar parameters), which gives an electron density distribution free of any thermal contributions. The static deformation density in the plane of the aromatic ring is shown in Fig. 4.

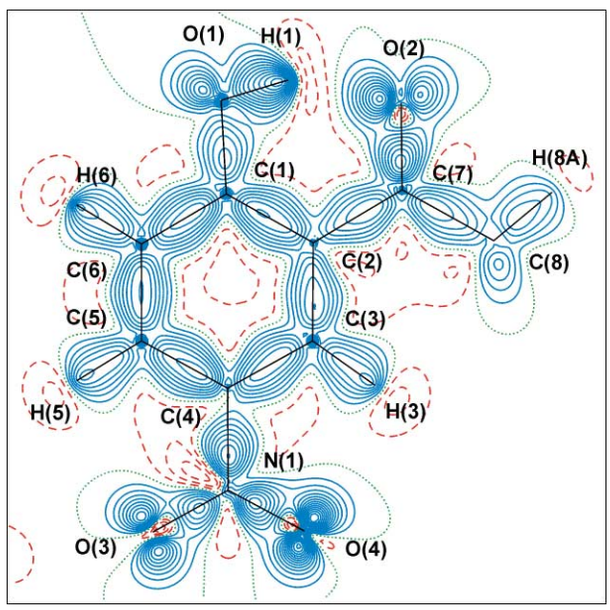

Fig. 4 Static deformation density in **1**. Contours as in Fig. 3.

The most evident features in Fig. 4 are the clear bonding densities in all covalent bonds with no discernible double maxima. Furthermore, the lone pair densities on the four oxygen atoms appear quite distinctly in this map. The deformation density appears slightly greater in the lone pairs on O(4) than on O(3), possibly due to the torsion angle C(3)–C(4)–N(1)–O(4) = +3.7°. Similarly, the density in the two lone pairs on O(2) is asymmetric, with the largest concentration of electron density on the side of O(2) towards H(1) in the intramolecular hydrogen bond. This group also deviates from the mean plane of the molecule by 4.5°. These features can be illustrated more clearly, when the Laplacian of $\rho(\boldsymbol{r})$ is plotted. Fig. 5 details the experimental Laplacian map. A more elaborate analysis of the lone pair geometry and hydrogen bonds will be presented in the next section.

A more recent and quantitative method of assessing the interatomic bonding, is the topological analysis of the electron density using the Atoms In Molecules (AIM) approach.[18] The results of this analysis for **1** of both the experimental and theoretical charge densities are given in Table 3.

Overall, the correspondence between the theoretical and the experimental topological analyses is quite reasonable. The average difference in ρ_{bcp} is 0.16 e Å^{-3}, while in $\nabla^2\rho_{bcp}$ this value is 5.8 e Å^{-5}. The largest differences appear in the heteropolar N–O and C–O bonds (6.6 e Å^{-5} and 34.6 e Å^{-5}respectively). This effect has been seen in previous charge density refinements[25] and this discrepancy is due to the limited flexibility on the radial parameters employed in the multipole refinement procedure. In general, the experimental values for ρ_{bcp} are higher than the corresponding theoretical results, while no

Table 3 Topological analysis of the electron density in the covalent bonds[a]

$Bond_{1-2}$	Model	ρ/e Å^{-3}	$\nabla^2\rho/e$ Å^{-5}	ε	d_{1-2}/Å	$d_{1\text{-bcp}}$/Å	$d_{2\text{-BCP}}$/Å
N(1)–O(3)	Opt	3.36	−25.1	0.11	1.226	0.583	0.643
	Exp	3.55(3)	−18.5(1)	0.14	1.233	0.598	0.636
N(1)–O(4)	Opt	3.35	−24.9	0.11	1.227	0.584	0.643
	Exp	3.56(2)	−13.2(1)	0.07	1.235	0.606	0.630
C(1)–O(1)	Opt	2.11	−10.00	0.01	1.330	0.453	0.877
	Exp	2.34(2)	−22.19(8)	0.11	1.342	0.545	0.797
C(2)–C(1)	Opt	1.99	−19.02	0.20	1.426	0.691	0.735
	Exp	2.12(2)	−19.01(4)	0.28	1.423	0.704	0.720
C(6)–C(5)	Opt	2.14	−21.62	0.22	1.378	0.680	0.699
	Exp	2.22(1)	−20.30(1)	0.30	1.384	0.692	0.692
C(7)–O(2)	Opt	2.63	−4.4	0.03	1.233	0.420	0.814
	Exp	2.94(2)	−39.0(1)	0.12	1.241	0.471	0.771
C(8)–C(7)	Opt	1.72	−14.92	0.04	1.509	0.725	0.784
	Exp	1.78(2)	−13.06(4)	0.19	1.501	0.718	0.783
H(1)–O(1)	Opt	2.24	−55.8	0.02	0.991	0.186	0.805
	Exp	3.00(9)	−52.1(6)	0.06	1.002	0.276	0.726
H(5)–C(5)	Opt	1.93	−24.37	0.01	1.082	0.375	0.706
	Exp	1.81(1)	−18.73(1)	0.09	1.089	0.361	0.728
H(8A)–C(8)	Opt	1.88	−22.67	0.01	1.088	0.388	0.700
	Exp	1.79(3)	−17.53(9)	0.01	1.084	0.334	0.750
H(8B)–C(8)	Opt	1.83	−21.59	0.01	1.094	0.396	0.698
	Exp	1.71(2)	−15.29(4)	0.07	1.082	0.344	0.738
H(8C)–C(8)	Opt	1.83	−21.59	0.01	1.094	0.396	0.698
	Exp	1.67(2)	−14.01(4)	0.03	1.086	0.345	0.741
C(2)–C(3)	Opt	2.05	−19.94	0.20	1.400	0.694	0.706
	Exp	2.03(2)	−16.81(4)	0.36	1.403	0.679	0.724
C(2)–C(7)	Opt	1.83	−16.36	0.13	1.479	0.730	0.748
	Exp	1.85(2)	−15.72(4)	0.23	1.478	0.711	0.767
C(3)–H(3)	Opt	1.94	−24.31	0.01	1.081	0.705	0.376
	Exp	1.80(2)	−18.27(7)	0.09	1.095	0.731	0.364
C(3)–C(4)	Opt	2.13	−21.61	0.23	1.383	0.680	0.703
	Exp	2.17(2)	−19.66(4)	0.26	1.390	0.701	0.689
C(4)–C(5)	Opt	2.07	−20.56	0.19	1.401	0.717	0.684
	Exp	2.19(2)	−18.98(4)	0.31	1.404	0.715	0.688
C(6)–H(6)	Opt	1.91	−23.57	0.02	1.083	0.700	0.383
	Exp	1.84(1)	−19.37(1)	0.08	1.081	0.723	0.358
C(6)–C(1)	Opt	2.07	−20.85	0.21	1.407	0.673	0.734
	Exp	2.20(2)	−20.95(4)	0.31	1.407	0.716	0.692
C(4)–N(1)	Opt	1.75	−16.11	0.16	1.469	0.563	0.905
	Exp	1.89(2)	−16.87(8)	0.17	1.457	0.545	0.912

[a] Opt refers to the B3LYP/6-311++G** optimised structure, Exp experimentally determined values.

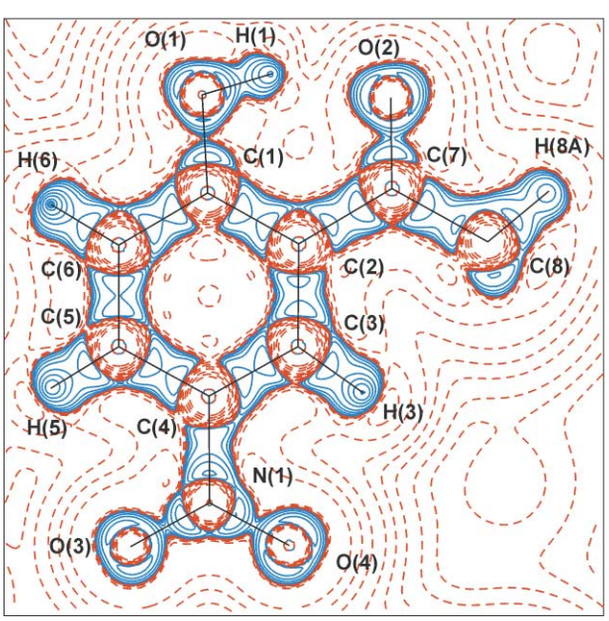

Fig. 5 Negative Laplacian of $\rho(\boldsymbol{r})$ in the same plane as Fig. 4. Contours shown are ±0.001 and ±2, ±4, ±8 × 10^n e Å^{-5}, $n = -3, -2, -1, 0, 1, 2, 3$. Solid lines show positive contours, dashed lines show negative contours. Zero contour not shown.

trend is observed for $\nabla^2\rho_{\text{bcp}}$. The values of the ellipticities in the covalent bonds suggest that a significant amount of π-bonding is present throughout the molecule (with the exception of the C–H and O–H bonds). The two delocalised N–O bonds show almost identical values of ρ, however, the bond to O(4) gives a slightly smaller ellipticity and a less negative $\nabla^2\rho_{\text{bcp}}$, This suggests that this bond has a little more single bond character than the N–O(3) bond.

Theoretical calculations allow us to calculate the covalent bond order directly, using the method proposed by Ángyán.[26] These show bond orders slightly greater than unity for the O(1)–C(1) bond (1.02), while the N(1) bonds to O(3) and O(4) has its covalent order calculated to be 1.64 and 1.63 respectively. This, combined with the value for the C(4)=N(1) bond of 0.87 points to an overall picture of polarised, but still strongly covalent N=O bonds. The slightly lower value for C(7)=O(2) (1.35) may result from the stronger H-bonding in which this atom is involved (see below). This influence can clearly be seen in the O(1)–H(1) bond where the effect of the strong intramolecular hydrogen bonding is to lower this bond order to 0.48. The homopolar C_{ar}=C_{ar} bond has an average order of 1.33, while for C_{ar}–H and C_{sp_3}–H the values are 0.92 and 0.94 respectively.

Analysis of the hydrogen bonding

The crystal structure of **1** contains a variety of hydrogen bonds ranging from strong to very weak in strength. The geometry of the hydrogen bonds in the crystal structure of **1** are given in Table 4, while Table 5 contains the topological parameters of all the hydrogen bonds (HBs) in **1**, for which a bcp could be located. The O(1)–H(1) ··· O(2) HB is significantly stronger

Table 4 Hydrogen bonding geometry in **1** [Å, °]

Bond	d(H ⋯ O)	d(X ⋯ O)	∠ X–H ⋯ O
O(1)–H(1) ⋯ O(2)	1.648(2)	2.572(1)	151.6(1)
C(5)–H(5) ⋯ O(3)	2.419(1)	2.737(1)	94.9(1)
C(5)[a]–H(5)[a] ⋯ O(2)	2.184(1)	3.268(1)	173.8(1)
C(6)[b]–H(6)[b] ⋯ O(4)	2.240(1)	3.307(1)	168.9(1)
C(8)[c]–H(8A)[c] ⋯ O(4)	2.552(1)	3.629(1)	172.5(1)
O(1)–H(1) ⋯ O(3)[a]	2.628(1)	3.139(1)	111.7(1)
C(8)–H(8B) ⋯ O(3)[d]	2.732(1)	3.321(1)	113.9(1)
C(8)–H(8C) ⋯ O(3)[e]	2.763(1)	3.710(1)	145.7(1)
C(3)–H(3) ⋯ O(4)	2.341(1)	2.737(1)	94.9(1)

[a] 1/2 − x, y − 1, −1/2 + z. [b] 1/2 + x, 1 − y, z. [c] 1 − x, −y, 1/2 + z. [d] x, −1 + y, z. [e] 1 − x, 1 − y, −1/2 + z.

than the other HBs, signified both by its shorter distance (d(H ⋯ O) = 1.648(2) Å) and the topological parameters. As described in the experimental section, the description of the electron density of H(1) needed the inclusion of quadrupoles (l_{max} = 2). The effect of this is shown in Fig. 6, which shows the Laplacian of the density in the plane of this HB.

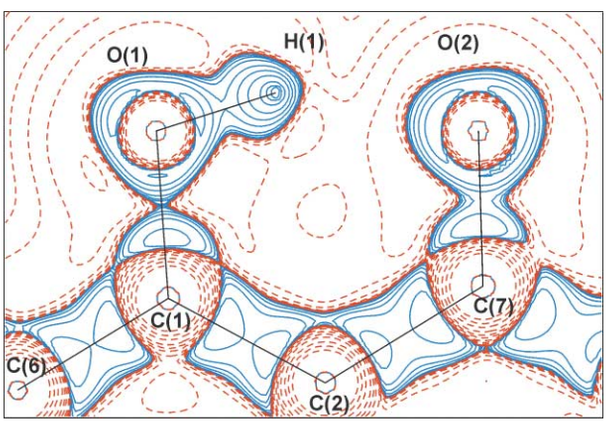

Fig. 6 Negative Laplacian of the intramolecular O(1)–H(1) ⋯ O(2) hydrogen bond. Contours as in Fig. 5.

The valence shell charge concentration (VSCC) on H(1) is slightly polarised towards O(2), indicating that this HB is significantly stronger than normal, purely electrostatic HBs. Distortion of the spherical VSCC around hydrogens has been observed in stronger HBs,[27] which has been interpreted as the intermediate in the transition of hydrogen to a position midway between the donor and acceptor atoms.

Another important thing to note in Table 5 is the absence of a HB cp between O(4) and H(3) and the presence of such a bond between O(3) and H(5). This is surprising as the former atoms are separated by 2.314(2) Å while d(O(3)–H(5)) is 2.419(2) Å. This may be explained by differences in the additional intermolecular interactions to the two oxygens. O(4) is involved in one short C–H–O HB,[28] while all intermolecular interactions to O(3) are much weaker. It is worth noting, however, that the C(5)–H(5)–O(3) HB has a very bent character (∠C(5)–H(5)–O(3) = 94.9(1)°).

Table 6 Energy densities in hydrogen bonds [hartree e^{-1} for G, V, H; hartree Å^{-3} for G/ρ]

Bond	G	V	H	G/ρ
H(1) ⋯ O(2)	+0.29	−0.33	−0.04	0.88
H(5) ⋯ O(3)	+0.09	−0.06	+0.03	1.12
H(5)[a] ⋯ O(2)	+0.08	−0.05	+0.03	1.92
H(6)[b] ⋯ O(4)	+0.06	−0.03	+0.03	1.88
H(8A)[c] ⋯ O(4)	+0.03	−0.02	+0.01	1.17
H(1) ⋯ O(3)[a]	+0.02	−0.01	+0.01	0.82
H(8B) ⋯ O(3)[d]	+0.03	−0.02	+0.01	0.80
H(8C) ⋯ O(3)[e]	+0.02	−0.01	+0.01	0.98

[a] 1/2 − x, y − 1, −1/2 + z. [b] 1/2 + x, 1 − y, z. [c] 1 − x, −y, 1/2 + z. [d] x, −1 + y, z. [e] 1 − x, 1 − y, −1/2 + z.

Energy densities in the hydrogen bonds

The energy densities in the HBs can be determined experimentally using the functional suggested by Abramov.[29] The results are given in Table 6. G is the kinetic energy density, V the potential energy density and H is the sum of G and V. The kinetic energy density is proportional to the ionic character of the chemical bond, while the potential energy density concerns the covalency. Extensive correlation studies of HBs have revealed a number of empirical relationships between the topological parameters and the energy density parameters, which in turn have been related to the bonding energies.[30] For the H(1) ⋯ O(2) intramolecular hydrogen bond we see that the values for both G and V are greater than for the other weak hydrogen bonds. What is interesting to note here is that there is a greater covalent contribution in this the stronger bond, whereas the ionic contribution seems to carry the greater weight in the remaining weaker hydrogen bonds.

The potential energy density correlation gives a bonding energy of the H(1) ⋯ O(2) intramolecular HB of 64.2 kJ mol^{-1} (this is at the lower end of the energy range for strong hydrogen bonds given as between 50–100 kJ mol^{-1}).[31] The bonding energies of the much weaker C–H–O HBs can also be calculated from the values in Table 7. These give values of 11.7, 9.7, 5.9, kJ mol^{-1} for H(5) ⋯ O(3), H(5) ⋯ O(2) and H(6) ⋯ O(4) respectively. This is in reasonable accord with the values calculated for C–H ⋯ O(nitro) HBs of 15 kJ mol^{-1}.[32] The very weak nature of the remaining HB's is illustrated by an average bond energy of *ca.* 3.0 kJ mol^{-1}.

Source contributions to the intramolecular hydrogen bond

The strength of the intramolecular HB of H(1) can further be analysed by calculating the source function contributions[33] at the hydrogen bond critical point, $S(\mathbf{r}_{bcp})$ (Table 7). This has previously been introduced in the analysis of hydrogen bonds in

Table 5 Topological analysis of hydrogen bonds

Bond	ρ_{bcp}/e Å^{-3}	$\nabla^2\rho_{bcp}/e$ Å^{-5}	$R_{1\text{-bcp}}$/Å	$r_{2\text{-bcp}}$/Å	λ_1/e Å^{-5}	λ_2/e Å^{-5}	λ_3/e Å^{-5}
H(1)–O(2)[a]	0.32(5)	3.5(1)	0.526	1.133	−3.10	−2.52	9.12
	0.37	3.5	0.537	1.108			
H(5)–O(3)	0.08(1)	1.64(1)	1.114	1.344	−0.27	−0.16	2.07
H(5)[b]–O(2)	0.04(1)	1.60(1)	0.788	1.421	−0.15	−0.12	1.87
H(6)[c]–O(4)	0.03(1)	1.23(1)	0.841	1.435	−0.13	−0.09	1.45
H(8A)[d]–O(4)	0.03(1)	0.61(1)	1.008	1.550	−0.08	−0.07	0.76
H(1)–O(3)[b]	0.02(1)	0.37(1)	1.503	1.592	−0.11	−0.07	0.54
H(8B)–O(3)[e]	0.04(1)	0.57(1)	1.272	1.537	−0.10	−0.05	0.71
H(8C)–O(3)[f]	0.02(1)	0.37(1)	1.164	1.630	−0.06	−0.06	0.49

[a] Second line gives the B3LYP/6-311++G** value. [b] 1/2 − x, y − 1, −1/2 + z. [c] 1/2 + x, 1 − y, z. [d] 1 − x, −y, 1/2 + z. [e] x, −1 + y, z. [f] 1 − x, 1 − y, −1/2 + z.

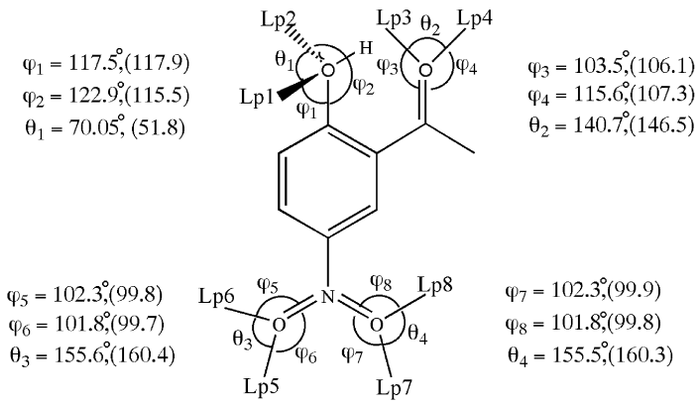

Fig. 7 Angular orientation of the (3, −3) LP's in **1**. Theoretical values are given in parentheses.

Table 7 Atomic source function contributions to the intramolecular hydrogen bond from B3LYP/6-311++G** wavefunction [e Å^{-3}]

Atom	$S(r_{bcp})$	% of total
O(1)	+0.0195	37.5
O(2)	+0.0165	31.8
H(1)	−0.0006	−1.2
All atoms	+0.0519	100
Value[a]	+0.0516	

[a] ρ from optimised wavefunction.

Table 8 Lone pair (LP) (3, −3) critical point data for **1**[a]

Lone pair	d/Å	ρ/e Å^{-3}	$\nabla^2\rho_{bcp}/e$ Å^{-5}
LP1–O(1)	0.343	6.23	−129.37
	0.342	6.24	−112.44
LP2–O(1)	0.342	6.55	−138.91
	0.342	6.26	−113.28
LP3–O(2)	0.337	6.88	−162.31
	0.339	6.53	−128.82
LP4–O(2)	0.340	6.27	−137.35
	0.343	6.33	−122.42
LP5–O(3)	0.333	6.90	−160.58
	0.337	6.72	−141.45
LP6–O(3)	0.332	6.91	−164.44
	0.337	6.75	−141.70
LP7–O(4)	0.332	6.91	−164.44
	0.337	6.70	−140.01
LP8–O(4)	0.333	6.88	−160.33
	0.337	6.73	−140.97

[a] The data presented on second line refer to the values determined from the B3LYP/6-311++G** calculation.

an organic complex[34] showing a clear trend in the change from weak to stronger hydrogen bonds. In ref. 34, it was concluded that an increase in HB strength is accompanied with an increase in $S(r_{bcp})$ from the involved hydrogen atomic basin. In **1**, the source contributions to the intramolecular HB from the two oxygen atoms are approximately equal with only a slight bias towards O(1). The contribution from H(1) is negative however, which is an indication of a weak hydrogen bond.

Non-bonded charge concentrations

The lone pairs on the four oxygen atoms were located by a search for local maxima (so-called (3, −3) critical points) in the Laplacian function[18] (Table 8). Comparing the experimentally determined values with those from the experimental geometry calculated wavefunction, we can see that the agreement for the radial distances is excellent, with a maximum discrepancy of 0.005 Å. There are small discrepancies seen when comparing the values of ρ from the experimental to the theoretical, however the values are still realistic, with an average discrepancy of 0.17 e Å^{-3}. The values for $\nabla^2\rho$ are consistently overestimated when compared to the theoretical values. As the Laplacian is a very rapidly changing function, its value is highly dependent on the determined radial position (d) of the (3, −3) cp, with even a small shift in d resulting in a markedly different value for the experimental result. What is encouraging however, is that both values of ρ and $\nabla^2\rho$ do show internal consistency in the experimental model, whether it be over- or under-estimated.

Considering now solely the experimental values, it is clear from this table that there are discrepancies in the values of the charge density in the LPs on O(2), compared to the two other sp^2-hybridised oxygen atoms O(3) and O(4). The lone pair angular positions are shown schematically in Fig. 7. There is certainly a small degree of difference between the experimental result and those calculated from theory. This is particularly evident in the θ angle for the two LP's on O(1), however the values are still within the expected range. The O_{sp^2} atoms LP angular positions all have good agreement to those calculated with a maximum discrepancy of 8.3°. What is interesting to note is the angle involving LP4, which is the LP on O(2) that points away from H(1), is significantly larger than the other LPs on the sp^2-hybridised oxygens. Similarly, ρ and $\nabla^2\rho$ are much lower for this LP. These discrepancies indicate strongly that there is a polarisation of the density on O(2), which is also evident from Fig. 6. We suggest that this deformation of the valence shell of O(2) is caused by this atom's involvement in the intramolecular HB. The sp^3 hybridisation of O(1) can be seen from the sum of the inter LP and LP-bond angles (310.5°), clearly indicating a pyramidal arrangement of these lone pairs.

Intermolecular interaction energy

The intermolecular interaction energies derived from the charge density parameters[35] provide insight about the strength of different types of interactions within the crystal structure. Dispersion forces are exerted through π–π interactions, while electrostatic forces are also high due to the relatively large dipole moment of the molecule. The dipole moment of one single molecule in the crystalline environment is 9.2(6) D, compared to the gas-phase dipole moment of 3.5 D, an enhancement of as much as 157%; a result of the large amount of weak intermolecular interactions in the molecule. The large crystal field enhancement of the molecular dipole moment in **1** suggests that electrostatic forces should predominate in any intermolecular interactions. Here we find that the calculated lattice energy is −166.0(6) kJ mol^{-1}, where electrostatic, exchange/repulsion and dispersion terms contribute −175, 155, −145 kJ mol^{-1} respectively. Thus it is the electrostatic term that dominates, but clearly not as much as might be first anticipated from the rather large experimental dipole moment.

Electrostatic potential

A useful application of the multipole model is the ability

to derive the molecular electrostatic potential (MEP) for an isolated molecule in the crystalline environment, and hence to evaluate contributions of electrostatics to intermolecular interactions and the lattice stabilization. Fig. 8a shows the theoretical map as both negative (purple) and positive (blue) regions of this property, at the ±0.03 au isosurface value. Fig. 8b shows the experimental as both negative (purple: −0.2 *e* Å^{-1}) and positive (blue: +0.5 *e* Å^{-1}) regions of this property of **1**. It is apparent that the negative electrostatic potential is concentrated mainly around the NO_2 group in the theoretical map, but is significantly reduced in the experimental, a feature commonly observed due to the nature of increased intermolecular interactions. What is interesting to note however is that the negative area of O(2) has disappeared from the experimental map at this isosurface level. This was intriguing, so in an attempt to mimic simply the hydrogen bonding motif present in the crystal, we carried out a gas-phase DFT optimisation of **1** involving hydrogen bonding a small molecule (in this case HF) to the O(2) atom. What we found was that including an intermolecular hydrogen bond changed the electrostatic nature of O(2), reducing its EP (electrostatic potential) by approximately 0.1 au, and producing a complete lack of negative EP on O(2) at the same isosurface level. This is entirely consistent with what we see in Fig. 8b. Thus H-bonding clearly masks much of the electronegative character of O(2), tying it up in the intramolecular interaction and preventing it from attracting an external positive charge/electrophile. What is also interesting to note is the polarisation of the negative EP of O(1) away from the intramolecular HB. When compared to the experimental MEP this apparent difference is far more pronounced. This can be attributed to the fact that in the crystal the oxygen atom is involved in no significant intermolecular hydrogen bonds. The rest of the molecule in the main, has positive electrostatic potential.

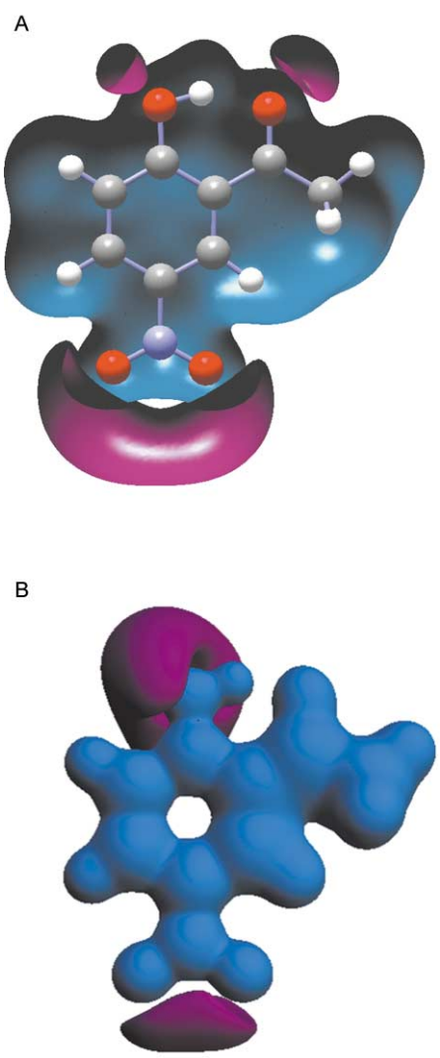

Fig. 8 Theoretical MEP in **1** at the −0.03 au (purple), and +0.03 au (blue), isosurface levels. Experimental MEP in **1** at the −0.2 (purple), and +0.5 *e* Å^{-1} (blue), isosurface levels.

Table 9 Atomic charges in **1** [*e*]

Atom	qP_v (κ-ref)	qMSK [a]
O(1)	−0.71(5)	−0.612
O(2)	−0.39(4)	−0.584
O(3)	−0.26(4)	−0.451
O(4)	−0.35(4)	−0.461
N(1)	+0.36(6)	+0.778
C(1)	+0.18(3)	+0.538
C(2)	−0.01(4)	−0.398
C(3)	+0.04(4)	−0.113
C(4)	−0.04(4)	−0.007
C(5)	−0.09(3)	−0.141
C(6)	−0.05(4)	−0.284
C(7)	+0.37(4)	+0.759
C(8)	−0.13(4)	−0.534
H(1)	+0.27(3)	+0.489
H(3)	+0.13(2)	+0.168
H(5)	+0.13(2)	+0.188
H(6)	+0.13(2)	+0.199
H(8A)	+0.15(1)	+0.162
H(8B)	+0.15(1)	+0.157
H(8C)	+0.15(1)	+0.157
SUM	+0.00	+0.010

[a] From B3LYP/6-311++G** wavefunction.

Atomic charges

The atomic charges can be derived from a charge density analysis in a number of ways. A crude and very straightforward way is to take the monopole values from a κ-refinement as a measure of the atomic charge. The MEP can also be used to derive a set of atomic partial charges, using the scheme proposed by Mertz *et al.*[36] which reproduce the potential outside the molecule and hence compactly describe it. These Mertz–Singh–Kollman (MSK) charges, reported in Table 9, follow the same pattern as those derived from monopole populations, both definitions agreeing on the broad picture of negative oxygens and positive nitrogen, though the actual values vary considerably within this.

Concentrating on qP_v, the different chemical environment of the carbon atoms is also reflected in the atomic charges. C(2) is bonded to the highly positive C(7) thus retaining a negative charge, while C(1) is bonded to the electronegative O(1). The larger positive charge on C(1) is therefore expected. C(3) appears as an anomaly by being positive while its 'chemically equivalent' atoms C(5) and C(6) are both negative. C(4) is negative as one would expect when bound to the highly positive N(1) atom, and C(7) has a large positive charge associated with it as it is bonded to two highly negative atoms C(8) and O(2).

Conclusions

We have determined the high-resolution electron density distribution of 1-(2-hydroxy-5-nitrophenyl)ethanone using a model based around the standard multipole formalism, and compared the results throughout with the analogous properties determined by theoretical calculation. These studies indicate that there is no evidence for the presence of keto–enol tautomerisation, and hence resonance assisted hydrogen bonding in this molecule. Topological analysis has been used to describe the degree of π-delocalisation throughout, and reveals that the intramolecular hydrogen bond is not as strong as would have originally been expected. However, the estimated bond energy justifies its characterisation as a weak to medium

strength hydrogen bond. The electronic source contributions from the oxygen atoms involved towards this hydrogen bond are approximately equal, and is certainly assisted by the polarisation of the carbonyl lone pair. The intramolecular hydrogen bond is shown to have a pronounced effect on the distribution of the molecular electrostatic potential around the carbonyl oxygen atom, and hence the likely reactivity of the molecule.

Acknowledgements

We would like to thank Dr Jane R. Hanrahan (Faculty of Pharmacy, U.Syd) for supplying the crystalline samples for both diffraction experiments and Ms Margaret Whitton for some technical assistance. We would also like to thank the Australian Research Council for funding this work, the Australian Institute for Nuclear Science and Engineering for supporting the neutron diffraction experiment, and the Australian Centre for Advanced Computing and Communications for a generous allocation of computational resources. JO would like to thank the Danish Research Council for financial support.

References

1 P. Pietta, *J. Nat. Prod.*, 2000, **63**, 1035–1042.
2 (*a*) E. Middleton Jr and C. Kandaswami, *Biochem. Pharmacol.*, 1992, **43**, 1167–1179; E. Middleton Jr, *Adv. Exp. Med. Biology.*, 1998, **439**, 175–182; P. A. Berg and P. T. Daniel, *Prog. Clin. Biol. Res.*, 1988, **280**, 157–171.
3 S. Kuo, *Adv. Exp. Med. Biol.*, 2002, **59**, 191–200.
4 R. J. Gryglewski, J. Robak and J. Swies, *NATO ASI Ser. A; Life Sci.*, 1985, **95**, 149–66.
5 (*a*) T. M. Kitson and K. E. Kitson, *Biochim. Biophys. Acta*, 2000, **1481**, 247–254; H. Bormann and M. F. Melzig, *Pharmazie*, 2000, **55**, 129–132.
6 (*a*) J. H. Medina, H. Viola, C. Wolfman, M. Marder, C. Wasowski, D. Calvo and A. C. Paladini, *Phytomedicine*, 1998, **5**, 235–243; M. Chebib and G. A. R. Johnston, *J. Med. Chem.*, 2000, **43**, 1427–1447.
7 (*a*) W. W. Cleland and M. M. Kreevoy, *Science*, 1994, **264**, 1887–1890; (*b*) P. A. Frey, S. A. Whitt and J. B. Tobin, *Science*, 1994, **264**, 1927–1930; (*c*) J. B. Tobin, S. A. Whitt, C. S. Cassidy and P. A. Frey, *Biochemistry*, 1995, **34**, 6919–6924; (*d*) M. Garcia-Viloca, A. Gonzalez-Lafont and J. M. Lluch, *J. Am. Chem. Soc.*, 1997, **119**, 1081–1086; (*e*) M. A. McAllister, *Can. J. Chem.*, 1997, **75**, 1195–1202; (*f*) Y. Pan and M. A. McAllister, *J. Am. Chem. Soc.*, 1997, **119**, 7561–7566; (*g*) Y. Pan and M. A. McAllister, *J. Am. Chem. Soc.*, 1998, **120**, 166–169; (*h*) C. J. Smallwood and M. A. McAllister, *J. Am. Chem. Soc.*, 1997, **119**, 11277–11281; (*i*) Y. Pan and M. A. McAllister, *J. Org. Chem.*, 1997, **62**, 8171–8176; (*j*) J. A. Platts and K. E. Laidig, *J. Phys. Chem.*, 1996, **100**, 13455–13461; (*k*) M. E. Tuckerman, D. Marx, M. L. Klein and M. Parrinello, *Science*, 1997, **275**, 817–820; (*l*) A. Warshel, A. Papazyan and P. A. Kollman, *Science*, 1995, **269**, 102–104.
8 C. J. Reid, *J. Chem. Phys.*, 1959, **30**, 182–190.
9 E. D. Stevens, M. S. Lehmann and P. Coppens, *J. Am. Chem. Soc.*, 1977, **99**, 2829–2831.
10 (*a*) C. Flensburg, S. Larsen and R. F. Stewart, *J. Phys. Chem.*, 1995, **99**, 101310–10141; P. R. Mallinson, K. Wozniak, G. T. Smith and K. L. McCormack, *J. Am. Chem. Soc.*, 1994, **116**, 909–915; P. Roversi, M. Barzaghi, F. Merati and R. Destro, *Can. J. Chem.*, 1996, **74**, 1145–1161; G. K. H. Madsen, B. B. Iversen, F. K. Larsen, M. Kapone, G. M. Reisner and F. H. Herbstein, *J. Am. Chem. Soc.*, 1998, **120**, 10040–10045.
11 (*a*) G. Gilli, F. Bellucci, V. Ferretti and V. Bertolasi, *J. Am. Chem. Soc.*, 1989, **111**, 1023–1028; (*b*) P. Gilli, F. Bellucci, V. Ferretti, V. Bertolasi, *Advances in Molecular Structure Research*, ed. M. Hargittai, and I. Hargittai, JAI Press, Greenwich, CT, 1996, Vol. 2, 67–102.
12 Bruker, SMART, SAINT+ and XPREP. Area detector control, data integration and reduction software. Bruker Analytical X-ray Instruments Inc., Madison, WI, USA, 1995.
13 R. H. Blesssing, *J. Appl. Crystallogr.*, 1989, **22**, 396.
14 http://www.ansto.gov.au/ansto/neut/2tana.html.
15 G. M. Sheldrick, SHELXL-97, Program for crystal structure refinement, University of Göttingen, Germany, 1997.
16 M. J. Frisch, G. W. Trucks, H. B. Schlegel, G. E. Scuseria, M. A. Robb, J. R. Cheeseman, V. G. Zakrzewski, J. A. Montgomery Jr., R. E. Stratmann, J. C. Burant, S. Dapprich, J. M. Millam, A. D. Daniels, K. N. Kudin, M. C. Strain, O. Farkas, J. Tomasi, V. Barone, M. Cossi, R. Cammi, B. Mennucci, C. Pomelli, C. Adamo, S. Clifford J. Ochterski, G. A. Petersson, P. Y. Ayala, Q. Cui, K. Morokuma, D. K. Malick, A. D. Rabuck, K. Raghavachari, J. B. Foresman, J. Cioslowski, J. V. Ortiz, A. G. Baboul, B. B. Stefanov, G. Liu, A. Liashenko, P. Piskorz, I. Komaromi, R. Gomperts, R. L. Martin, D. J. Fox, T. Keith, M. A. Al-Laham, C. Y. Peng, A. Nanayakkara, C. Gonzalez, M. Challacombe, P. M. W. Gill, B. Johnson, W. Chen, M. W. Wong, J. L. Andres, C. Gonzalez, M. Head-Gordon, E. S. Replogle, J. A. Pople, *Gaussian 98*, Revision A. 7, Gaussian, Inc., Pittsburgh PA, 1998.
17 (*a*) A. D. Becke, *J. Chem. Phys.*, 1993, **98**, 5648–5652; (*b*) C. Lee, W. Yang and R. G. Parr, *Phys. Rev. B.*, 1988, **37**, 785–789; (*c*) P. J. Stevens, F. J. Devlin, C. F. Chabalowski and M. J. Frisch, *J. Phys. Chem.*, 1994, **98**, 11623–11627; (*d*) C. Adamo and V. Barone, *Chem. Phys. Lett.*, 1997, **274**, 242–250.
18 R. F. W. Bader, *Atoms in Molecules: a Quantum Theory*, Clarendon Press, Oxford, 1990.
19 http://www.ac3.com.au/sgi-origin-2400.htm.
20 G. M. Sheldrick, SHELX-86. Program for crystal structure solution, University of Göttingen, Germany, 1986.
21 N. K. Hansen and P. Coppens, *Acta Crystallogr., Sect. A.*, 1979, **39**, 909–921.
22 T. Kortisanszky, S. T. Howard, P. R. Mallinson, Z. Su, T. Richter and N. K. Hansen, XD—a computer program package for the multipole refinement and analysis of electron densities from diffrraction data. Free University of Berlin, 1997.
23 *International Tables of Crystallography, Vol. C*, ed. A. J. C. Wilson, Kluwer Academic Publishers, Dordrecht, 1992, pp. 500–502; 219–222; 193–199.
24 E. Clementi and D. L. Raimondi, *J. Chem. Phys.*, 1963, **38**, 2686–2689.
25 A. Volkov and P. Coppens, *Acta Crystallogr., Sect A*, 2001, **A57**, 395–405.
26 J. G. Ángyán, M. Loos and I. Mayer, *J. Phys. Chem.*, 1994, **98**, 5244–5248.
27 G. K. H. Madsen, B. B. Iversen, F. K. Larsen, M. Kapon, G. M. Resiner and F. H. Herbstein, *J. Am. Chem. Soc.*, 1998, **120**, 10040–10045.
28 T. Steiner, *Crystallogr. Rev.*, 1996, **6**, 1–57 . In this review, the H–O separations in the C–H–O HBs are in the range from 2.22 to 2.62 Å.
29 Yu. A. Abramov, *Acta Crystallogr. Sect. A.*, 1997, **53**, 264–272.
30 (*a*) E. Espinosa, C. Lecomte and E. Molins, *Chem. Phys. Lett.*, 1999, **300**, 745–748; (*b*) E. Espinosa, M. Souhassou, H. Lachekar and C. Lecomte, *Acta Crystallogr., Sect. B*, 1999, **55**, 563–572; (*c*) E. Espinosa, E. Molins and C. Lecomte, *Chem. Phys. Lett.*, 1998, **285**, 170–173.
31 F. Hibbert and J. Emsley, *Adv. Phys. Org. Chem.*, 1990, **26**, 255–379.
32 F. H. Allen, C. A. Baalham, J. P. M. Lommerse, P. R. Raithby and E. Sparr, *Acta Crystallogr., Sect. B*, 1997, **53**, 1017–1024.
33 R. F. W. Bader and C. Gatti, *Chem. Phys Lett.*, 1998, **287**, 233–238.
34 J. Overgaard, B. Schiøtt, F. K. Larsen and B. B. Iversen, *Chem. Eur. J.*, 2001, **7**, 3756–3767.
35 Yu. A. Abramov, A. Volkov, G. Wu and P. Coppens, *Acta Crystallogr., Sect. A*, 2000, **56**, 585–591.
36 (*a*) U. C. Sing and P. A. Kollman, *J. Comput. Chem.*, 1984, **5**, 129–145; (*b*) B. H. Bezler, K. M. Mertz and P. A. Kollman, *J. Comput. Chem.*, 1990, **11**, 431–439.